

Article

Theoretical Methodology of a High-Flux Coal-Direct Chemical Looping Combustion System

Xiaojia Wang ^{1,*}, Xianli Liu ^{1,2}, Zhaoyang Jin ¹, Jiewen Zhu ¹ and Baosheng Jin ¹

¹ Key Laboratory of Energy Thermal Conversion and Control of Ministry of Education, School of Energy and Environment, Southeast University, Nanjing 210096, China; liuxl_seu@163.com (X.L.); zhaoyangjinseu@163.com (Z.J.); jiewenzhuseu@163.com (J.Z.); bsjin@seu.edu.cn (B.J.)

² China Energy Engineering Group Jiangsu Power Design Institute Co. Ltd., Nanjing 211102, China

* Correspondence: xiaojiaawang@seu.edu.cn; Tel.: +86-025-8379-2811

Received: 26 October 2018; Accepted: 30 November 2018; Published: 4 December 2018



Abstract: This study, as an extension of our previous experimental tests, presented a mechanism analysis of air reactor (AR) coupling in a high-flux coal-direct chemical looping combustion (CDCLC) system and provided a theoretical methodology to the system optimal design with favorable operation stability and low gas leakages. Firstly, it exhibited the dipleg flow diagrams of the CDCLC system and concluded the feasible gas–solid flow states for solid circulation and gas leakage control. On this basis, the semi-theoretical formulas of gas leakages were proposed to predict the optimal regions of the pressure gradients of the AR. Meanwhile, an empirical formula of critical sealing was also developed to identify the advent of circulation collapse so as to ensure the operation stability of the whole system. Furthermore, the theoretical methodology was applied in the condition design of the cold system. The favorable gas–solid flow behaviors together with the good control of gas leakages demonstrated the feasibility of the theoretical methodology. Finally, the theoretical methodology was adopted to carry out a capability assessment of the high-flux CDCLC system under a hot state in terms of the restraint of gas leakages and the stability of solid circulation.

Keywords: coal-direct chemical looping combustion; coupling mechanism; theoretical methodology; high-flux; gas leakage; pressure gradient

1. Introduction

Coal-direct chemical looping combustion (CDCLC) has been demonstrated as an attractive combustion technology of coal with the inherent feature for CO₂ capture [1,2]. The CDCLC concept is typically implemented in two interconnected reactors, the so-called fuel reactor (FR) and the air reactor (AR), with an oxygen carrier (OC) circulating in between to transfer oxygen and heat. Specifically, in the FR, the fuel is first devolatilized and gasified by the gasification agent steam, and then the gasification products (mainly CO, H₂, and CH₄) are further oxidized to CO₂ and H₂O by the OC. In the AR, the reduced OC from the FR is oxidized by the air for regeneration, and then will be recirculated back to the FR. By means of the OC particles that deliver oxygen from the AR to FR, the direct mixing of the fuel and air can be avoided, and further highly purified CO₂, without the dilution of N₂, can be acquired at the outlet of the FR via the condensation of steam [3–12].

Alternatively, a characterized CDCLC system consisting of a high-flux circulating fluidized bed (HFCFB) riser as the FR and a counter-flow moving bed (CFMB) as the AR was proposed in our previous studies [13–15], as shown in Figure 1. The main advantages of this design are that the HFCFB FR can provide high solids concentration over the whole reactor height for favorable gas–solid contact efficiency and reaction performance, and that the CFMB AR possesses steady solids flow and low-pressure drop. Besides, an inertial separator, connecting the two reactors, was specially designed

as the carbon stripper to separate the coarse OC particles off the FR into the AR for regeneration, and also recirculate the fine particles of the unconverted coal char back to the FR for further conversion.

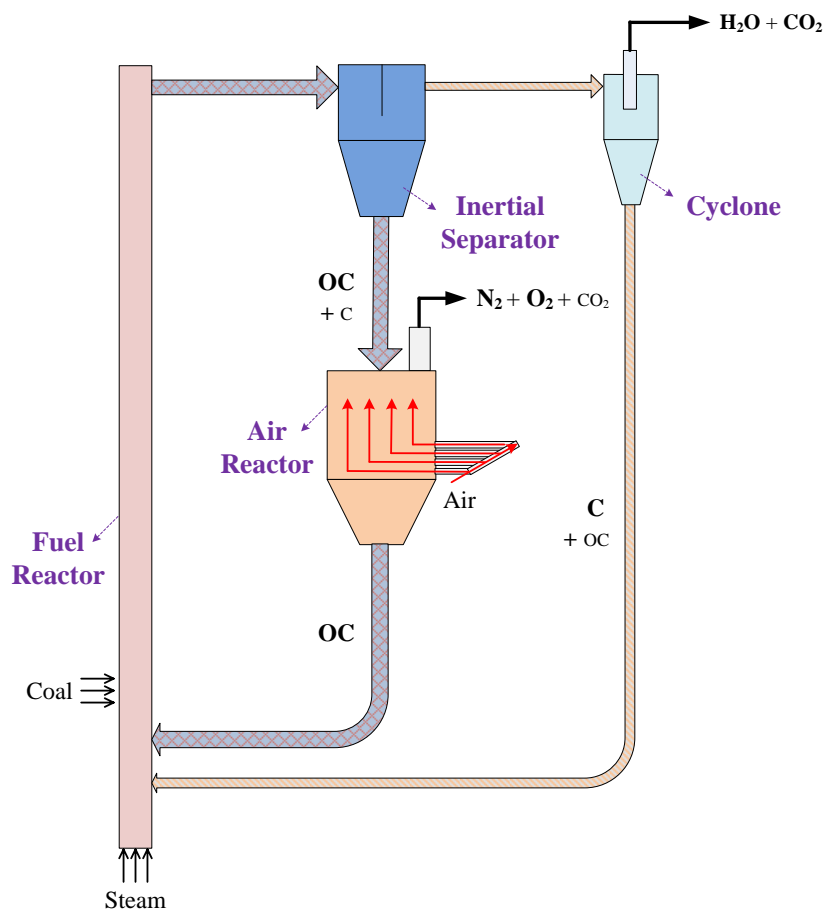


Figure 1. Schematic of the high-flux coal-direct chemical looping combustion (CDCLC) system (OC: oxygen carrier).

Up to now, we have successively developed cold [14] and pilot-scale hot [15] experimental systems of this high-flux CDCLC concept, preliminarily realizing the whole-system stable operation with acceptable gas–solid reaction performance under certain conditions. Similar feasibility studies have been experimentally conducted in different pilot-scale CDCLC units, e.g., the 10 kW_{th} [3] and 100 kW_{th} [9] units at Chalmers University of Technology (Sweden), the 10 kW_{th} [4] and 50 kW_{th} [5] units at Southeast University (China), the 1 MW_{th} unit from Technische Universität Darmstadt (Germany) [10], the 25 kW_{th} unit at Hamburg University of Technology (Germany) [11], the 25 kW_{th} unit from Ohio State University (America) [12], the 50 kW_{th} unit at Instituto de Carboquímica (ICB-CSIC) (Spain) [16], and the 5 kW_{th} CDCLC reactor at Huazhong University of Science and Technology (China) [17]. However, despite promising experimental results obtained in pilot-scale units, the CDCLC technology for CO₂ capture has to be further developed towards large-scale commercial applications. In this aspect, it is essential to develop theoretical methodologies, beside experimental studies, for a better understanding of hydrodynamic and reaction mechanisms in CDCLC processes, which can provide vital references to the design, operation, and process optimization of the future large-scale CDCLC power plants. By far, compared to the extensive experimental studies, few studies are available in the literature on the development of theoretical methodologies in terms of hydrodynamics and/or reaction mechanisms for CDCLC processes. Su et al. [18], based on the hydrodynamic equations for fluidized beds and the reaction kinetics, simulated the CDCLC process in a dual circulating fluidized bed (DCFEB) system. Ohlemüller et al. [19] developed a process

simulation model to predict the flow and reaction performances of a 1 MW_{th} unit at Technische Universität Darmstadt.

In our previous experimental tests, we have found that the coupling of the CFMB AR into the downcomer of the HF CFB FR makes the hydrodynamic mechanism of the whole system much more complicated, and hence leads to crucial effects on the operation independence of the two reactors (i.e., FR and AR) in terms of solid circulation stability and gas leakages [20]. In this context, it is necessary to carry out an in-depth mechanism investigation of this high-flux CDCLC system coupled by a CFMB AR, which is significant to the design and operation processes of the future CDCLC applications. Therefore, the objective of this study is to develop a theoretical methodology to illustrate the fundamental hydrodynamics of our high-flux CDCLC system, extending from the previous experimental studies. The main contributions of this work are listed as follows: (1) the screening of the feasible gas–solid flow states for solid circulation and gas leakage control on the strength of the dipleg flow diagrams of the CDCLC system; (2) the development of the semi-theoretical formulas of gas leakages to predict the optimal regions of the pressure gradients of the AR; (3) the development of the empirical formula of critical sealing to identify the advent of circulation collapse so as to ensure the whole-system operation stability; (4) the feasibility validation of the theoretical methodology through its application in the cold-state condition design; (5) the successful application of the theoretical methodology into the capability assessment of the high-flux CDCLC system under a hot state, in terms of the restraint of gas leakages and the stability of solid circulation.

2. Materials and Methods

2.1. Visualization Experimental Device

The visualization experimental device of the high-flux CDCLC system consists primarily of a FR, an inertial separator, a downcomer, an AR, and a J-valve. During the operation process, the FR, with an inner diameter of 60 mm and a height of 5.8 m, was operated in dense suspension upflow (DSU) regime with high solid circulation flux and solids holdup. An inertial separator was installed following the FR, and was used as the carbon stripper to separate the gas stream and elutriated particles off the FR. The particle outlet of the inertial separator was connected with the downcomer, and further the AR which was operated in moving bed regime with an inner diameter of 418 mm and a height of 0.7 m. After leaving the AR, the OC particles were transported back to the FR with the help of the J-valve. The drawing presented in Figure 2 schematically shows how the different sections of the visualization experimental setup are interconnected. The more detailed description can be found in our previous experimental studies with this system [14,20].

The tracer gas (99.99% CO) concentrations were continuously measured with a gas analyzer (MRU, Neckarsulm, Germany) at the outlets of the two reactors. The pressures were measured with pressure gages and a multi-channel differential pressure transducer. The gas flow rates were adjusted and measured by calibrated rotameters (Changzhou shuanghuan thermal instrument co., LTD, Changzhou, China) and then normalized to the standard state (labeled with a subscript *sta*). Specifically, $Q_{1,sta}$, $Q_{2,sta}$, $Q_{3,sta}$, and $Q_{4,sta}$ represent the inlet air flow rate of the FR, the fluidizing air flow rate of the J-valve, the aeration air flow rate of the J-valve, and the inlet air flow rate of the AR, respectively. $Q_{a,sta}$ and $Q_{b,sta}$ represent the outlet air flow rates of the FR and the AR, respectively.

2.2. Materials

The OC material used in this study was a natural iron ore from Harbin, China with an average particle diameter of 0.43 mm and bulk density of 1577 kg/m³. The minimum fluidization gas velocity under the cold condition was 0.187 m/s [20].

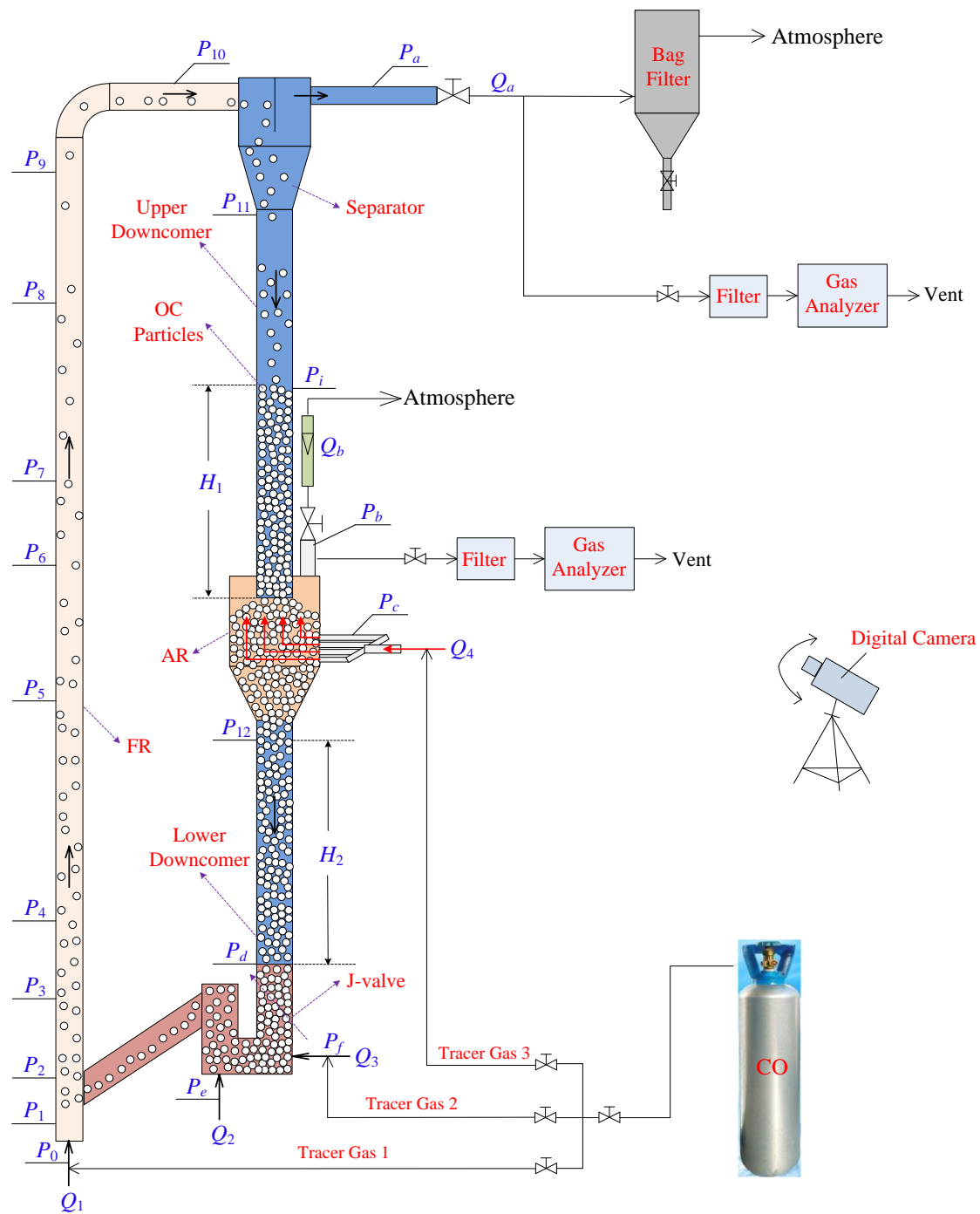


Figure 2. Schematic diagram of the cold-state experimental device of the high-flux CDCLC system.
P: pressure; *Q*: gas flow; AR: air reactor; FR: fuel reactor.

2.3. Performance Indicators

The upper pressure gradient ($\Delta P_1/H_1$) represents the pressure gradient between the AR and the carbon stripper, which was expressed as Equation (1). The lower pressure gradient ($\Delta P_2/H_2$) represents the pressure gradient between the J-valve and the AR, which was expressed as Equation (2) [20].

$$\Delta P_1/H_1 = \left(\frac{p_b + p_c}{2} - p_i \right) / H_1 \quad (1)$$

$$\Delta P_2/H_2 = (p_d - p_{12}) / H_2 \quad (2)$$

Solid circulation flux, G_s , represents the solid circulation ratio (kg/s) per unit area of the FR, which was estimated by [20,21]

$$G_s = \frac{\rho_b u_s A_{ud}}{A_f} = \frac{\rho_b A_{ud}}{A_f} (\Delta H/t) \quad (3)$$

The solids holdup in the FR, ε_s , could be estimated according to the local pressure drop [13,14,21–24].

$$\Delta P_Z / \Delta Z \approx [\rho_s \varepsilon_s + \rho_g (1 - \varepsilon_s)]g \quad (4)$$

The FR leakage ratio, f_1 , represents the gas leakage ratio from the FR to the AR. During the experimental process, the FR leakage ratio was measured by using tracer gas 1 [14,20].

$$f_1 = -\frac{Q_{b,sta} x_{b,CO}}{Q_{a,sta} x_{a,CO} + Q_{b,sta} x_{b,CO}} \quad (5)$$

In this study, the upward direction is defined as the positive direction, and hence the FR leakage ratio should be negative.

The AR leakage ratio, f_2 , represents the gas leakage ratio from the AR to the FR, which could be measured by using tracer gas 2 [14,20].

$$f_2 = \frac{Q_{a,sta} x'_{a,CO}}{Q_{a,sta} x'_{a,CO} + Q_{b,sta} x'_{b,CO}} \quad (6)$$

The J-valve leakage ratio, f_3 , represents the gas leakage ratio of the J-valve aeration air into the AR, which was measured by using tracer gas 3 [20].

$$f_3 = \frac{Q_{b,sta} x''_{b,CO}}{Q_{a,sta} x''_{a,CO} + Q_{b,sta} x''_{b,CO}} \quad (7)$$

The detailed meanings of the symbols can be found in the nomenclature.

3. Results and Discussion

3.1. Gas–Solid Flow Characteristics

In typical circulating fluidized bed (CFB) reactors, the downcomer dipleg plays a critical role in solid circulation and gas seal. In order to drive particles, the whole dipleg is usually kept in a state of negative pressure gradient (i.e., a decrease of pressure with the increase of downcomer height) [25–31]. However, the coupling of the AR into the downcomer of our high-flux CDCLC system together with the special requirements of gas leakages makes the operation mechanism of the dipleg and even the whole system much more complicated. As shown in Figure 2, the existence of the AR divides the dipleg into the upper dipleg and the lower dipleg. During the CDCLC process, the lower dipleg stays at a negative pressure gradient state with the J-valve owning the maximum pressure so as to drive the solids for circulation. But the upper dipleg can situate at a pressure region across the positive and negative pressure gradient states, which has crucial effects on the circulation stability and gas leakage ratios. Therefore, a systematic study is necessary to improve the understanding of AR coupling effects on the hydrodynamic mechanism of this CDCLC system in terms of solid circulation stability and gas leakage controllability.

Figure 3 shows the possible gas–solid flow states in the upper dipleg during the high-flux CDCLC process, where the upward direction is defined as the positive direction [32]. As the abovementioned discussions, the upper dipleg flow can be categorized into seven flow states, according to the differential pressure between the two ends of the upper dipleg. In the first state, the top pressure of the upper dipleg is much larger than that at the bottom, and the gas flow moves downward with a much higher

velocity than that of the solids. The big velocity difference between the gas–solid phases means the dramatic CO₂ leakage from the carbon stripper into the AR, and hence the great reduction of CO₂ capture efficiency. In the second state, the positive differential pressure between the top and bottom becomes much smaller, and the gas velocity is only slightly higher than the solids velocity, indicating a modest gas leakage from the FR to the AR. In the third state, when the differential pressure between the two ends of the upper dipleg becomes zero, the solids downward flow is controlled by gravity and the gas–solid relative velocity becomes zero. Then in the fourth state, the bottom pressure of the upper dipleg starts to outpace the top pressure, and the gas–solid flow becomes negative pressure gradient flow, leading to a further reduction of the downward velocity of gas phase. When the downward gas velocity further decreases to zero, it comes to the fifth state, so-called the ideal sealing state. At this point, the gas–solid relative velocity is equal to the absolute value of the solids descending velocity, indicating the ideal suppression of the gas leakages between the FR and AR. In the sixth state, with the further enhancement of the negative pressure gradient, the gas begins to flow upward with a low velocity, indicating a small amount of gas leakage from the AR to the FR. Finally, when a large amount of gas flow moves upward in terms of visible large bubbles, the upper dipleg will enter into the last state, so-called the critical sealing state, meaning that the whole-system particle circulation is about to be broken together with a dramatical leakage of N₂ from the AR into FR. In general, States 1 and 2 belong to the positive pressure gradient flow, State 3 belongs to the zero pressure gradient flow, and States 4 to 7 belong to the negative pressure gradient flow.

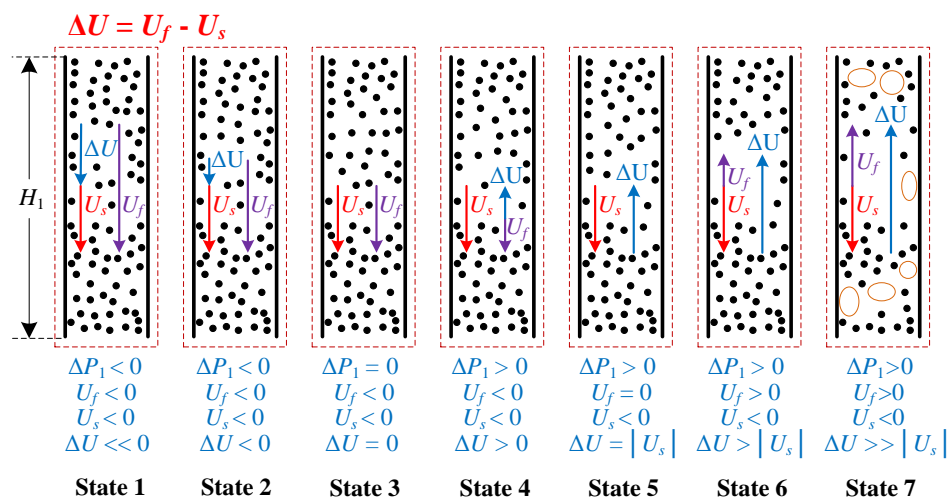


Figure 3. Gas–solid flow diagrams in the upper dipleg under different pressure gradient conditions.

Our previous experimental studies found that with the increase of the upper pressure gradient $\Delta P_1/H_1$, the FR leakage ratio f_1 had a linear drop until extinction while the AR leakage ratio f_2 firstly stayed at zero and then had a linear increase [20]. Thus, the variations of gas–solid flow state in the upper dipleg corresponding to the upper pressure gradient could be further deduced, as shown in Figure 4. It can be found that the gas flow direction in the upper dipleg changed from downward to upward. By referring to Figure 3, it can be concluded that the gas–solid flow in the upper dipleg had gone through States 2 to 6, demonstrating the feasibility of the selection of optimal operation region for the gas leakage control and solid circulation by means of the adjustment of the upper pressure gradient $\Delta P_1/H_1$. Consistent with the experimental studies [20], we set -3% and 3% as the limit values of the two gas leakages f_1 and f_2 , respectively, and as the selection criteria of the upper pressure gradient. Thus, we can get the optimal region of $\Delta P_1/H_1$ corresponding to States 2 to 6 under the involved operation conditions: State 2 ($-2.1 \text{ kPa/m} < \Delta P_1/H_1 < 0 \text{ kPa/m}$), State 3 ($\Delta P_1/H_1 = 0 \text{ kPa/m}$), State 4 ($0 \text{ kPa/m} < \Delta P_1/H_1 < 1.6 \text{ kPa/m}$), State 5 ($\Delta P_1/H_1 = 1.6 \text{ kPa/m}$), and State 6 ($1.6 \text{ kPa/m} < \Delta P_1/H_1 < 3.0 \text{ kPa/m}$).

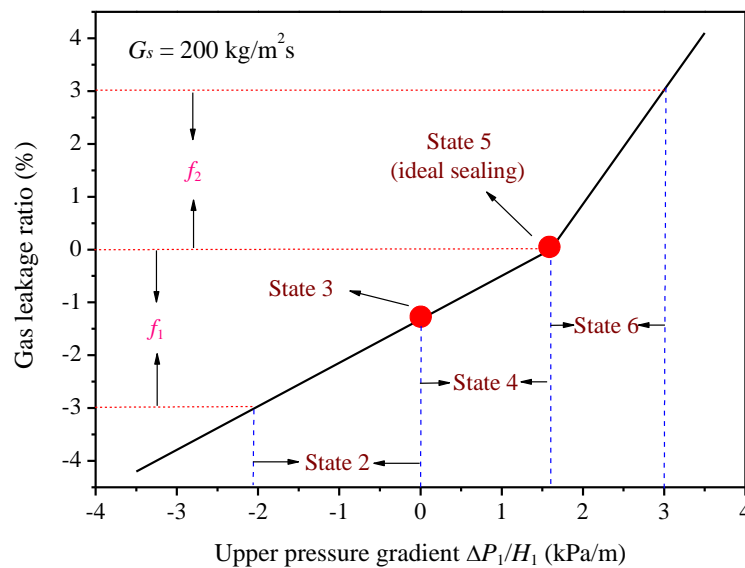


Figure 4. Variations of gas–solid flow state in the upper dipleg with the upper pressure gradient.

On the other hand, as mentioned above, because the J-valve is the driving source for solid circulation, it has the maximum pressure of the whole system. Hence, the lower dipleg necessarily stays at a negative pressure gradient region, i.e., States 4 to 7 as shown in Figure 3. However, considering that the gas leakage from the AR to the J-valve will result in the mixing of N_2 into the FR, and further the reduction of CO_2 capture concentration, State 4 should also better be avoided during the CDCLC process. Moreover, an excess gas leakage (i.e., State 7 shown in Figure 3) will cause serious damage on the stability of the solids downward flow, and further the solid circulation. Therefore, only States 5 and 6 were regarded as the preferred gas–solid flow states in the lower dipleg. Consistent with our previous experimental studies [20], we set 20% as the upper limit value of the gas leakage f_3 , and as the selection criterion of optimal region under the involved operation conditions.

3.2. Theoretical Methodology for Gas Leakage Restraint

3.2.1. Semi-Theoretical Formulas of the Upper Pressure Gradient

From the analyses made above, we can find that the coupling of the CFMB AR makes the gas–solid flow in the upper dipleg very complicated, which covers a diversity of flow structures from positive pressure gradient to negative pressure gradient states. In a real CDCLC application, the optimal operation region should better locate among States 2 to 6 in order to acquire stable solid circulation and favorable restraint of gas leakages. Fortunately, we found that the optimal region exhibited a relatively symmetrical distribution rule with the ideal sealing state (i.e., State 5) as the core. Thus, it provides a possibility for us to propose an empirical equation applied to the high-flux CDCLC system based on the ideal sealing theory.

The modified Ergun equation was attempted to be applied in the stable moving bed flow of the upper dipleg under the ideal sealing state, which had the form of Equation (8) [33–35]. Meanwhile, according to the relationship between the solids velocity and solid circulation flux (see Equation (9)), we further got the correlation equation of the upper pressure gradient under the ideal sealing state with the solid circulation flux (i.e., Equation (10)).

$$(\Delta P_1/H_1)_i = 150 \frac{(1-\varepsilon)^2 \mu_g |U_s|}{(\varepsilon \varphi_s d_s)^2} + 1.75 \frac{(1-\varepsilon) \rho_g U_s^2}{\varepsilon \varphi_s d_s} \quad (8)$$

$$|U_s| = \left(\frac{D_f}{D_{ud}} \right)^2 \frac{G_s}{\rho_s (1-\varepsilon)} \quad (9)$$

$$(\Delta P_1/H_1)_i = \left[150 \frac{(1-\varepsilon)\mu_g}{\rho_s(\varepsilon\varphi_s d_s)^2} \left(\frac{D_f}{D_{ud}} \right)^2 \right] G_s + \left[1.75 \frac{\rho_g}{\varepsilon\varphi_s d_s (1-\varepsilon)\rho_s^2} \left(\frac{D_f}{D_{ud}} \right)^4 \right] G_s^2 \quad (10)$$

Figure 5 illustrates the comparison of predicted and experimental upper pressure gradients under the ideal sealing state (i.e., State 5). Table 1 lists the main parameters required for the calculation of the ideal upper pressure gradient. It can be seen that, with a solid circulation flux of 200 kg/m²·s, the value of the theoretical ideal pressure gradient was about 1.6 kPa/m which was almost the same with the experimental value. Then, when the solid circulation flux increased to 300 kg/m²·s, the theoretical and measured values of the ideal pressure gradient were increased to about 2.5 and 2.8 kPa/m, respectively. In general, the relative errors between the measured and predicted values of the ideal pressure gradient were kept to be lower than 15%, demonstrating the application feasibility of the modified Ergun equation in the prediction of the ideal pressure gradient of the high-flux CDCLC system.

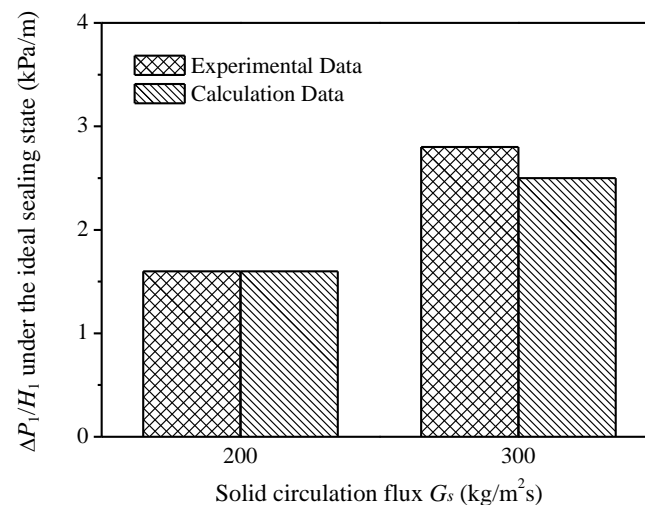


Figure 5. Comparison of predicted and experimental upper pressure gradients under ideal sealing states with different solid circulation fluxes.

Table 1. Parameters for the calculation of the ideal upper pressure gradient (OC: oxygen carrier; FR: fuel reactor).

Description	Value
Density of air ρ_g (kg/m ³)	1.29
Dynamic viscosity of air μ_g (Pa·s)	1.78×10^{-5}
Apparent density of the OC ρ_s (kg/m ³)	3015
Void fraction in the downcomer ε (-)	0.477
Mean diameter of the OC d_s (mm)	0.43
Sphere coefficient of the OC φ_s (-)	0.7
Diameter of the FR D_f (m)	0.06
Diameter of the upper downcomer D_{ud} (m)	0.10

In addition, from Figure 4, we can get the optimal region of the upper pressure gradient $\Delta P_1/H_1$ under a high-flux condition of 200 kg/m²·s, which ranged between -2.1 kPa/m and 3.0 kPa/m. Thus, by associating the optimal region with the ideal pressure gradient (1.6 kPa/m), a semi-theoretical formula of gas leakages between the two reactors (i.e., Equation (11)) could be deduced, which includes two conterminal linear equations with the ideal pressure gradient chosen as the boundary point. This formula successfully established the important mapping relationships between the gas–solid flow states in the upper dipleg and the upper pressure gradient, which should be important coupling criteria of selecting design parameters and operating conditions.

$$f_i = \begin{cases} f_1 = \alpha_1 [(\Delta P_1/H_1)_t - (\Delta P_1/H_1)_i] & ((\Delta P_1/H_1)_t < (\Delta P_1/H_1)_i, \alpha_1 \approx 0.8) \\ f_2 = \alpha_2 [(\Delta P_1/H_1)_t - (\Delta P_1/H_1)_i] & ((\Delta P_1/H_1)_t \geq (\Delta P_1/H_1)_i, \alpha_2 \approx 2.2) \end{cases} \quad (11)$$

3.2.2. Semi-Theoretical Formulas of the Lower Pressure Gradient

From the analyses shown in Section 3.1, we can find that the optimal operation region of the lower dipleg should better locate between State 5 (i.e., the ideal sealing state) and State 6 in order to ensure stable solid circulation with acceptable gas leakage.

The correlation equation of the lower pressure gradient under the ideal sealing state was also derived from the modified Ergun equation [33–35], as shown in Equation (12). Here, it should be noted that the lower downcomer was designed to be cuboid shaped (0.1 m length \times 0.1 m width) and the upper downcomer was cylinder shaped, which made the form of Equation (12) a bit different from that of Equation (10). Thus, the theoretical value of the ideal lower pressure gradient could be deduced to be about 1.3 kPa/m. Further, according to our previous experimental results [20], the optimal region of $\Delta P_2/H_2$ under a high-flux condition of 200 kg/m²·s should be limited within 6.0 kPa/m in order to guarantee the J-valve leakage ratio lower than 20%. Thus, by associating the optimal region of the lower pressure gradient with the ideal pressure gradient, a semi-theoretical formula of J-valve gas leakage (i.e., Equation (13)) could be deduced, in which the coefficient β was used as the slope. Similarly, with Equation (11), this formula established the mapping relationships between the J-valve gas leakage and the lower pressure gradient, enabling a coupling criterion of selecting design parameters and operating conditions during the CDCLC process.

$$(\Delta P_2/H_2)_i = \left[150 \frac{\pi}{4} \frac{(1-\varepsilon)\mu_g}{\rho_s(\varepsilon\varphi_s d_s)^2} \left(\frac{D_f}{L_{td}} \right)^2 \right] G_s + \left[1.75 \left(\frac{\pi}{4} \right)^2 \frac{\rho_g}{\varepsilon\varphi_s d_s (1-\varepsilon)\rho_s^2} \left(\frac{D_f}{L_{td}} \right)^4 \right] G_s^2 \quad (12)$$

$$f_3 = \beta [(\Delta P_2/H_2)_t - (\Delta P_2/H_2)_i] ((\Delta P_2/H_2)_t \geq (\Delta P_2/H_2)_i, \beta \approx 4.3) \quad (13)$$

3.3. Theoretical Methodology for Circulation Stability

In a real CDCLC application, a critical sealing state (i.e., State 7 shown in Figure 3) can be used to identify the advent of circulation collapse. Therefore, it is also necessary to understand the critical sealing ability of the CDCLC system so as to prevent the emergency situation of operation instability. Here, an empirical formula of critical sealing proposed by Chang et al. [32] (see Equation (14)) was attempted to be applied in this high-flux CDCLC system, in which the coefficient γ was between 0.6–0.7.

$$\left| \frac{\Delta P}{H} \right|_c = \gamma g_c [\rho_s (1-\varepsilon) - 136] \quad (14)$$

Figure 6 exhibits the comparison of predicted and experimental upper pressure gradients under the critical sealing state. It can be found that, with a solid circulation flux of 250 kg/m²·s, the experimental value of the critical sealing gradient was 10.7 kPa/m under an upper dipleg height of 1.07 m [20]. In order to ensure the accuracy of test measurement, another dipleg height (0.87 m) was adopted for the measure of the critical sealing gradient while the other operating conditions were kept constant. It can be seen that these two experimental results (10.9 kPa/m for 0.87 m height, and 10.7 kPa/m for 1.07 m height) were very close to each other, demonstrating the constancy of the critical sealing gradient. On the other hand, the calculation value of the critical sealing gradient based on Equation (14) was between 8.5 kPa/m and 9.9 kPa/m. Thus, the relative error between the measured and predicted values of the critical sealing gradient could be further calculated to be lower than 21% for γ of 0.6, and 8% for γ of 0.7, demonstrating the application feasibility of Chang et al. [32] equation in the prediction of the critical pressure gradient of the high-flux CDCLC system. Moreover, the value of 0.7 for the coefficient γ seems to be more suitable for this system, in view of the least

relative error with the experimental values. Therefore, the semi-theoretical formula for the circulation stability of this high-flux system can be finally expressed as Equation (15).

$$(\Delta P/H)_c = 0.7g_c[\rho_s(1 - \epsilon) - 136] \quad (15)$$

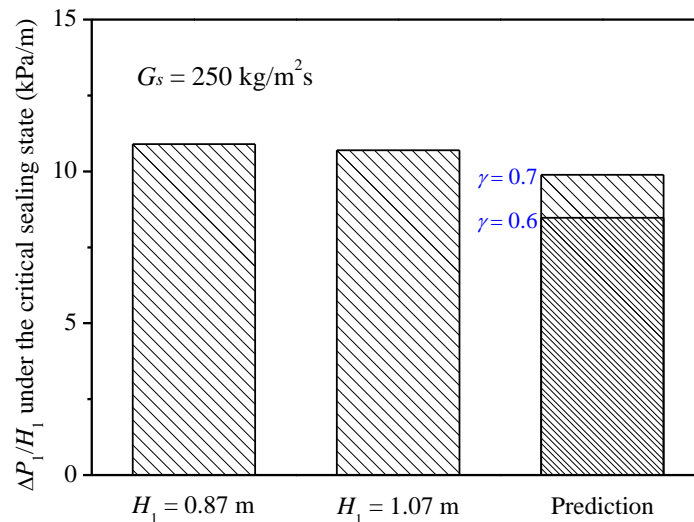


Figure 6. Comparison of predicted and experimental upper pressure gradients under the critical sealing state.

3.4. Theoretical Methodology Application to Condition Designs of the Cold System

Based on the theoretical methodology for the gas leakages and solid circulation, we proposed an optimal operation condition of the cold CDCLC system. Firstly, considering the feature and requirement of the high-flux operation, we selected a higher value of $300 \text{ kg/m}^2 \cdot \text{s}$ as the solid circulation flux G_s while the corresponding FR superficial gas velocity $U_{f,sta}$ and the inlet air flow rate of the AR $Q_{4,sta}$ were set to be 10.7 m/s and $44 \text{ m}^3/\text{h}$, respectively. Thus, according to Equations (10) and (12), the theoretical ideal pressure gradients of the upper dipleg and the lower dipleg should be about 2.5 kPa/m and 1.9 kPa/m , respectively. Then, on the basis of the above semi-theoretical formulas (i.e., Equations (11) and (13)), we could further deduce that the optimal regions for gas leakage restraint were about -1.3 to 3.9 kPa/m for the upper pressure gradient $\Delta P_1/H_1$, and about 1.9 to 6.6 kPa/m for the lower pressure gradient $\Delta P_2/H_2$. Under this premise, we selected 3.8 kPa/m and 5.2 kPa/m as the proposed values of $\Delta P_1/H_1$ and $\Delta P_2/H_2$, respectively.

Figure 7 exhibits the whole-system pressure profile and the apparent solids holdup along the FR height under the proposed operation condition. As shown in Figure 7a, the pressures of each part under the high-flux condition were smoothly connected with each other, demonstrating the operation stability and the favorable coupling between each component. Besides, the high-pressure drop in the FR and low-pressure drop in the AR, they successfully exhibited the operation features of HFCFB and CFMB. From Figure 7b, we further observed the high solids holdup along the whole FR height, indicating the positive effect of high solid circulation flux on the efficiencies of gas–solid contact and reaction [14]. In addition, Table 2 summarizes the pressure gradients and gas leakage ratios under the proposed operation condition. It can be found that, although the upper pressure gradient $\Delta P_1/H_1$ close to the upper limit of the optimal region, the FR leakage ratio f_1 (-0.1%) and the AR leakage ratio f_2 (2.5%) can still be limited within their limits (i.e., -3% for f_1 and 3% for f_2), demonstrating the feasibility of the semi-theoretical Equation (11) for the prediction of the optimal region for gas leakage control. On the other hand, the lower pressure gradient $\Delta P_2/H_2$ was located at a value of 5.2 kPa/m , in which the J-valve leakage ratio f_3 (15.2%) could be kept within a proposed region ($<20\%$) in order to ensure a favorable solid circulation.

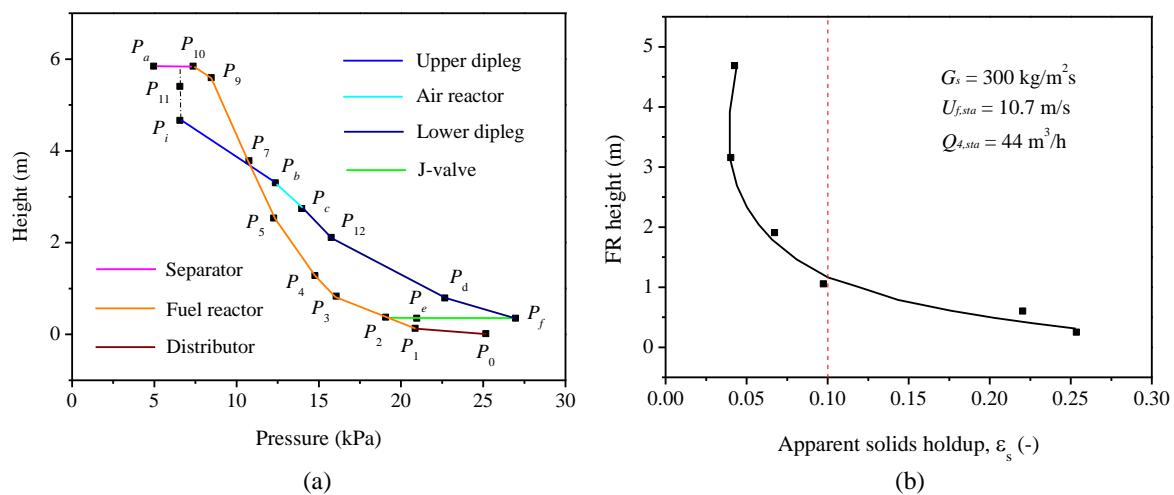


Figure 7. The pressure profile of the whole system and the apparent solids holdup along the FR under the proposed pressure gradient condition: (a) pressure profile, and (b) apparent solids holdup.

Table 2. Pressure gradients and gas leakage ratios under the proposed operation condition (AR: air reactor).

Description	Parameter	Measured Value (%)	Calculation Value (%)	Relative Error (%)
$\Delta P_1/H_1 = 3.8$ kPa/m	FR leakage ratio f_1	-0.1	0	-
	AR leakage ratio f_2	2.5	2.9	14
$\Delta P_2/H_2 = 5.2$ kPa/m	J-valve leakage ratio f_3	15.2	14.2	7

In general, the system operation stability, the high-flux feature, and particularly the gas leakage restraint were successfully achieved in this proposed operation condition, indicating the application feasibility of the semi-theoretical methodology to the system optimal design.

3.5. Hot State Application Assessment of the Theoretical Methodology

From the theoretical methodology of AR coupling principle with the high-flux CDCLC system, we could further carry out a capability assessment of the system in terms of the restraint of gas leakages and the stability of solid circulation under hot states. To facilitate the analysis and comparison, the structure parameters and OC material of the cold system were also adopted in the hot system. Besides, the solid circulation flux in the hot state was also selected as $300 \text{ kg/m}^2\cdot\text{s}$ so as to keep consistent with the proposed cold-state operation condition mentioned above. The only difference was that under the hot state, the operating temperature was as high as 1243 K with the corresponding dynamic viscosity $\mu_{g,hot} = 4.7 \times 10^{-5} \text{ Pa}\cdot\text{s}$. Table 3 details the parameters for the calculation of ideal pressure gradients under the hot state.

According to Equation (10), the theoretical ideal pressure gradient of the upper dipleg under the hot state should be about 6.4 kPa/m. Similarly, according to Equation (12), the theoretical ideal pressure gradient of the lower dipleg under the hot state was about 5.0 kPa/m. Figure 8 shows the comparison of the ideal pressure gradients between the hot and cold states. We can observe the ideal pressure gradients of the two diplegs under the hot state were about 2.6 times of those under the cold state. This implies a lower requirement of the sealing height in the hot state, which should be beneficial for the spatial arrangement of the hot-state system. In addition, on the basis of the semi-theoretical formulas for gas leakage restraint (i.e., Equations (11) and (13)), the optimal regions were further calculated to be about 2.7 to 7.8 kPa/m for $\Delta P_1/H_1$, and about 5 to 9.7 kPa/m for $\Delta P_2/H_2$. On the other hand, according to Equation (15), the critical pressure gradient for the circulation stability could be deduced to be about 9.9 kPa/m. It can be found that the upper limit of the optimal region of $\Delta P_2/H_2$

(9.7 kPa/m) for gas leakage restraint was very close to the critical pressure gradient for the circulation stability (9.9 kPa/m), demonstrating the rationality of the choice of 20% as the upper limit standard of the J-valve leakage. Certainly, it should be noted that the approach of the optimal pressure gradients for gas leakages to the critical pressure gradient for circulation stability also means the increase in the risk of circulation collapse during the hot-state operation process.

Table 3. Parameters for the calculation of the ideal pressure gradients under the hot state.

Description	Value
Temperature (K)	1243
Solid circulation flux G_s ($\text{kg}/\text{m}^2 \cdot \text{s}$)	300
Gas dynamic viscosity under the hot state $\mu_{g,hot}$ (Pa·s)	4.7×10^{-5}
Apparent density of the OC ρ_s (kg/m^3)	3015
Void fraction in the downcomer ε (-)	0.477
Mean diameter of the OC d_s (mm)	0.43
Sphere coefficient of the OC φ_s (-)	0.7
FR diameter D_f (m)	0.06
Upper downcomer diameter D_{ud} (m)	0.10
Side length of the lower downcomer L_{ld} (m)	0.10

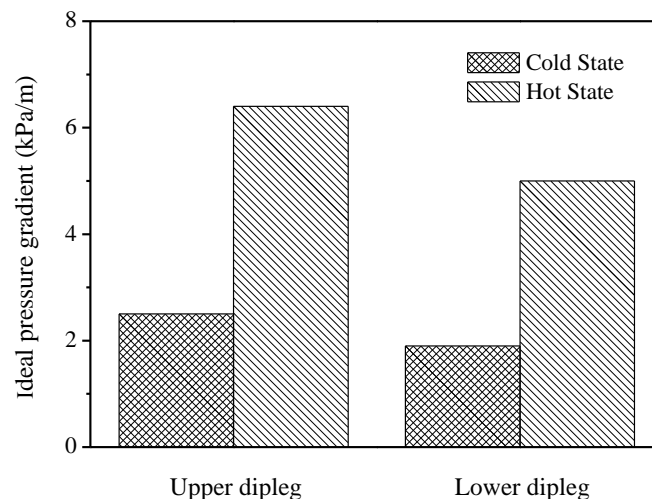


Figure 8. Comparison of the ideal pressure gradients between the hot and cold states.

For real high-flux CDCLC applications, we can first get the optimal sizes of the reactors and the downcomer based on the ideal pressure gradient equations and the solid circulation flux range in the design process. Then during the operating process, the relevant parameters (i.e., the solid-seal heights in the downcomer, the pressures of the FR and AR, the solid circulation flux, and the gas flow rates) can be adjusted flexibly and optimally to make sure the pressure gradients within the optimal regions for a favorable performance of operation and reaction.

4. Conclusions

Built upon the previous experimental studies of a high-flux CDCLC system, the objective of this study is to further investigate the fundamental coupling mechanism of the AR, and develop a comprehensive theoretical methodology to the system optimal design with favorable operation stability and low gas leakages. The following conclusions can be drawn from the present study:

- (1) During the CDCLC process, the dipleg flow can situate at a pressure region across the positive and negative pressure gradients, which can be categorized into seven flow states. Considering the gas leakages and the circulation stability, the upper dipleg of the AR was recommended

to be operated among State 2 to 6 while the lower dipleg of the AR should better run between States 5 and 6.

- (2) The gas leakages between the two reactors were expressed as two conterminal linear equations with the ideal pressure gradient chosen as the boundary point, which can be used to predict the optimal regions of the upper pressure gradient. Similarly, the J-valve leakage within the optimal region was expressed as a linear function of the lower pressure gradient of the AR. In addition, an empirical formula of critical sealing was developed for this high-flux CDCLC system, which can be used to identify the advent of circulation collapse so as to guarantee the operation stability.
- (3) The theoretical methodology for gas leakages and solid circulation was successfully applied to the condition design and operation of the cold system, achieving favorable gas–solid flow and circulation together with good control of gas leakages in the whole system.
- (4) The theoretical methodology was adopted to carry out a capability assessment of the high-flux CDCLC system under a hot state in terms of the restraint of gas leakages and the stability of solid circulation. The ideal pressure gradients under the hot state of 1243 K were about 2.6 times than those under the cold state, implying a lower requirement of sealing height in the hot state. However, on the other hand, the increase of the ideal pressure gradients also led to the approach of the optimal pressure gradients for gas leakages to the critical pressure gradients for circulation stability, which would increase the risk of circulation collapse during the operation process.

Author Contributions: conceptualization, X.W.; investigation, X.W. and X.L.; formal analysis, X.W. and X.L.; supervision, B.J.; writing—original draft preparation, X.W., X.L., and Z.J.; writing—review and editing, J.Z.

Funding: This research was funded by the National Natural Science Foundation of China (grant numbers 51806035, 51741603), the Natural Science Foundation of Jiangsu Province (grant number BK20170669), the Fundamental Research Funds for the Central Universities (grant number 2242018K40117), and the Guangdong Provincial Key Laboratory of New and Renewable Energy Research and Development (grant number Y707s41001).

Conflicts of Interest: The authors declare no conflict of interest.

Nomenclature

A_{ud}	sectional area of the upper downcomer (m^2)
A_f	sectional area of the upper FR (m^2)
d_s	mean diameter of the OC particles (mm)
D_f	FR diameter (m)
D_{ud}	upper downcomer diameter (m)
f_1	FR leakage ratio
f_2	AR leakage ratio
f_3	J-valve leakage ratio
f_i	gas leakage ratio between the two reactors ($i = 1$ or 2)
g	acceleration due to gravity ($9.8 m/s^2$)
g_c	conversion coefficient ($9.8 N/kg$)
G_s	solid circulation flux ($kg/m^2 \cdot s$)
H_1	solid-seal height of the upper dipleg of the AR (m)
H_2	solid-seal height of the lower dipleg of the AR (m)
ΔH	scale height in the upper dipleg of the AR (m)
L_{ld}	side length of the lower downcomer (m)
P_b	pressure of the AR outlet (kPa)
P_c	pressure of the AR inlet (kPa)
P_d	top pressure of the lower dipleg of the AR (kPa)
P_i	pressure at the interface of the dense phase and dilute phase of the upper downcomer (kPa)

P_{11}	pressure at the underside of the separator (kPa)
P_{12}	pressure at the top position of the lower dipleg (kPa)
ΔP_Z	local pressure drop at two adjacent elevations of the FR (kPa)
$(\Delta P/H)_c$	critical pressure gradient for circulation stability (kPa/m)
$\Delta P_1/H_1$	upper pressure gradient of the AR (kPa/m)
$(\Delta P_1/H_1)_i$	upper pressure gradient of the AR under the ideal sealing state (kPa/m)
$(\Delta P_1/H_1)_t$	transient upper pressure gradient of the AR (kPa/m)
$\Delta P_2/H_2$	lower pressure gradient of the AR (kPa/m)
$(\Delta P_2/H_2)_i$	lower pressure gradient of the AR under the ideal sealing state (kPa/m)
$(\Delta P_2/H_2)_t$	transient lower pressure gradient of the AR (kPa/m)
$Q_{1,sta}$	inlet air flow rate of the FR distributor (m^3/h)
$Q_{2,sta}$	fluidizing air flow rate of the J-valve (m^3/h)
$Q_{3,sta}$	aeration air flow rate of the J-valve (m^3/h)
$Q_{4,sta}$	inlet air flow rate of the AR (m^3/h)
$Q_{a,sta}$	outlet air flow rate of the FR (m^3/h)
$Q_{b,sta}$	outlet air flow rate of the AR (m^3/h)
t	measured duration of the OC particles passing through the scale height (s)
T	operation temperature (K)
u_s	velocity of the OC particles in the upper dipleg (m/s)
$U_{f,sta}$	FR superficial gas velocity (m/s)
U_s	solids velocity (m/s)
$x_{a,CO}$	concentration of tracer gas 1 measured at the outlet of the separator (ppm)
$x_{b,CO}$	concentration of tracer gas 1 measured at the AR outlet (ppm)
$x'_{a,CO}$	concentration of tracer gas 2 measured at the outlet of the separator (ppm)
$x'_{b,CO}$	concentration of tracer gas 2 measured at the AR outlet (ppm)
$x''_{a,CO}$	concentration of tracer gas 3 measured at the outlet of the separator (ppm)
$x''_{b,CO}$	concentration of tracer gas 3 measured at the AR outlet (ppm)
ΔZ	height difference between two adjacent elevations of the FR (m)
α_1	slope of the linear fitting equation of FR leakage ratio
α_2	slope of the linear fitting equation of AR leakage ratio
β	slope of the linear fitting equation of J-valve leakage ratio
γ	dimensionless coefficient of the fitting equation of critical sealing gradient
ε	void fraction in the downcomer
ε_s	cross-sectional average solids holdup in the FR
φ_s	sphere coefficient of the OC particles
ρ_b	bulk density of the OC particles (kg/m^3)
ρ_g	density of air (kg/m^3)
ρ_s	apparent density of the OC particles (kg/m^3)
μ_g	dynamic viscosity of air (Pa·s)

References

- Kim, H.R.; Wang, D.; Zeng, L.; Bayham, S.; Tong, A.; Chung, E.; Kathe, M.V.; Luo, S.; McGiveron, O.; Wang, A.; et al. Coal direct chemical looping combustion process: Design and operation of a 25-kWth sub-pilot unit. *Fuel* **2013**, *108*, 370–384. [[CrossRef](#)]
- Bayham, S.C.; Kim, H.R.; Wang, D.; Tong, A.; Zeng, L.; McGiveron, O.; Kathe, M.V.; Chung, E.; Wang, W.; Wang, A.; et al. Iron-based coal direct chemical looping combustion process: 200-h continuous operation of a 25-kWth subpilot unit. *Energy Fuels* **2013**, *27*, 1347–1356. [[CrossRef](#)]
- Berguerand, N.; Lyngfelt, A. Design and operation of a 10 kW_{th} chemical-looping combustor for solid fuels-testing with South African coal. *Fuel* **2008**, *87*, 2713–2726. [[CrossRef](#)]
- Shen, L.H.; Wu, J.H.; Xiao, J. Experiments on chemical looping combustion of coal with a NiO based oxygen carrier. *Combust. Flame* **2009**, *156*, 721–728. [[CrossRef](#)]
- Xiao, R.; Chen, L.; Saha, C.; Zhang, S.; Bhattacharya, S. Pressurized chemical-looping combustion of coal using an iron ore as oxygen carrier in a pilot-scale unit. *Int. J. Greenh. Gas Control* **2012**, *10*, 363–373. [[CrossRef](#)]

6. Abad, A.; Gayán, P.; de Diego, L.F.; García-Labiano, F.; Adánez, J. Fuel reactor modelling in chemical-looping combustion of coal: 1. Model formulation. *Chem. Eng. Sci.* **2013**, *87*, 277–293. [[CrossRef](#)]
7. García-Labiano, F.; de Diego, L.F.; Gayán, P.; Abad, A.; Adánez, J. Fuel reactor modelling in chemical-looping combustion of coal: 2-simulation and optimization. *Chem. Eng. Sci.* **2013**, *87*, 173–182. [[CrossRef](#)]
8. Wang, X.; Jin, B.; Zhang, Y.; Zhang, Y.; Liu, X. Three dimensional modeling of a coal-fired chemical looping combustion process in the circulating fluidized bed fuel reactor. *Energy Fuels* **2013**, *27*, 2173–2184. [[CrossRef](#)]
9. Markström, P.; Linderholm, C.; Lyngfelt, A. Operation of a 100 kW chemical-looping combustor with Mexican petroleum coke and Cerrejón coal. *Appl. Energy* **2014**, *113*, 1830–1835. [[CrossRef](#)]
10. Ströhle, J.; Orth, M.; Epple, B. Design and operation of a 1 MW_{th} chemical looping plant. *Appl. Energy* **2014**, *113*, 1490–1495. [[CrossRef](#)]
11. Thon, A.; Kramp, M.; Hartge, E.-U.; Heinrich, S.; Werther, J. Operational experience with a system of coupled fluidized beds for chemical looping combustion of solid fuels using ilmenite as oxygen carrier. *Appl. Energy* **2014**, *118*, 309–317. [[CrossRef](#)]
12. Bayham, S.; McGiveron, O.; Tong, A.; Chung, E.; Kathe, M.; Wang, D.; Zeng, L.; Fan, L.S. Parametric and dynamic studies of an iron-based 25-kW_{th} coal direct chemical looping unit using sub-bituminous coal. *Appl. Energy* **2015**, *145*, 354–363. [[CrossRef](#)]
13. Wang, X.; Jin, B.; Liu, X.; Zhang, Y.; Liu, H. Experimental investigation on flow behaviors in a novel in situ gasification chemical looping combustion apparatus. *Ind. Eng. Chem. Res.* **2013**, *52*, 14208–14218. [[CrossRef](#)]
14. Wang, X.; Jin, B.; Liu, H.; Wang, W.; Liu, X.; Zhang, Y. Optimization of in situ gasification chemical looping combustion through experimental investigations with a cold experimental system. *Ind. Eng. Chem. Res.* **2015**, *54*, 5749–5758. [[CrossRef](#)]
15. Wang, X.; Jin, B.; Zhu, X.; Liu, H. Experimental evaluation of a novel 20 kW_{th} in situ gasification chemical looping combustion unit with an iron ore as the oxygen carrier. *Ind. Eng. Chem. Res.* **2016**, *55*, 11775–11784. [[CrossRef](#)]
16. Adánez, J.; Abad, A.; Perez-Vega, R.; Luis, F.; García-Labiano, F.; Gayán, P. Design and operation of a coal-fired 50 kW_{th} chemical looping combustor. *Energy Procedia* **2014**, *63*, 63–72. [[CrossRef](#)]
17. Ma, J.; Zhao, H.; Tian, X.; Wei, Y.; Rajendran, S.; Zhang, Y.; Bhattacharya, S.; Zheng, C. Chemical looping combustion of coal in a 5 kW_{th} interconnected fluidized bed reactor using hematite as oxygen carrier. *Appl. Energy* **2015**, *157*, 304–313. [[CrossRef](#)]
18. Su, M.; Zhao, H.; Ma, J. Computational fluid dynamics simulation for chemical looping combustion of coal in a dual circulation fluidized bed. *Energy Convers. Manag.* **2015**, *105*, 1–12. [[CrossRef](#)]
19. Ohlemüller, P.; Alobaid, F.; Abad, A.; Adanez, J.; Ströhle, J.; Epple, B. Development and validation of a 1D process model with autothermal operation of a 1 MW_{th} chemical looping pilot plant. *Int. J. Greenh. Gas Control* **2018**, *73*, 29–41. [[CrossRef](#)]
20. Wang, X.; Liu, X.; Jin, B.; Wang, D. Hydrodynamic study of AR coupling effects on solid circulation and gas leakages in a high-flux in situ gasification chemical looping combustion system. *Processes* **2018**, *6*, 196. [[CrossRef](#)]
21. Wang, X.; Jin, B.; Zhong, W.; Zhang, M.; Huang, Y.; Duan, F. Flow behaviors in a high-flux circulating fluidized bed. *Int. J. Chem. React. Eng.* **2008**, *6*, A79. [[CrossRef](#)]
22. Issangya, A.S.; Bai, D.; Bi, H.T.; Lim, K.S.; Zhu, J.; Grace, J.R. Suspension densities in a high-density circulating fluidized bed riser. *Chem. Eng. Sci.* **1999**, *54*, 5451–5460. [[CrossRef](#)]
23. Namkung, W.; Kim, S.W.; Kim, S.D. Flow regimes and axial pressure profiles in a circulating fluidized bed. *Chem. Eng. J.* **1999**, *54*, 245–252. [[CrossRef](#)]
24. Li, Z.Q.; Wu, C.N.; Wei, F.; Jin, Y. Experimental study of high-density gas-solids flow in a new coupled circulating fluidized bed. *Powder Technol.* **2004**, *139*, 214–220. [[CrossRef](#)]
25. Jing, S.; Li, H. Study on the flow of fine powders from hoppers connected to a moving-bed standpipe with negative pressure gradient. *Powder Technol.* **1999**, *101*, 266–278. [[CrossRef](#)]
26. Nagashima, H.; Ishikura, T.; Ide, M. Flow characteristics of a small moving bed downcomer with an orifice under negative pressure gradient. *Powder Technol.* **2009**, *192*, 110–115. [[CrossRef](#)]
27. Wang, J.; Bouma, J.H.; Dries, H. An experimental study of cyclone dipleg flow in fluidized catalytic cracking. *Powder Technol.* **2000**, *112*, 221–228. [[CrossRef](#)]

28. Wang, Q.; Yang, H.; Wang, P.; Lu, J.; Liu, Q.; Zhang, H.; Wei, L.; Zhang, M. Application of CPFD method in the simulation of a circulating fluidized bed with a loop seal, part I—Determination of modeling parameters. *Powder Technol.* **2014**, *253*, 814–821. [[CrossRef](#)]
29. Wang, Q.; Yang, H.; Wang, P.; Lu, J.; Liu, Q.; Zhang, H.; Wei, L.; Zhang, M. Application of CPFD method in the simulation of a circulating fluidized bed with a loop seal Part II—Investigation of solids circulation. *Powder Technol.* **2014**, *253*, 822–828. [[CrossRef](#)]
30. Yin, S.; Jin, B.; Zhong, W.; Lu, Y.; Shao, Y.; Liu, H. Gas-solid flow behavior in a pressurized high-flux circulating fluidized bed riser. *Chem. Eng. Commun.* **2014**, *201*, 352–366. [[CrossRef](#)]
31. Wang, Z.; Zhao, T.; Yao, J.; Liu, K.; Takei, M. Influence of particle size on the exit effect of a full-scale rolling circulating fluidized bed. *Part. Sci. Technol.* **2018**, *36*, 541–551. [[CrossRef](#)]
32. Chang, G.; Yang, G.; Yang, S.; Li, S.; Li, H. Gas solid flow in a moving bed under negative pressure difference. *J. Chem. Ind. Eng.* **1980**, *31*, 229–240.
33. Ergun, S. Fluid flow through packed columns. *Chem. Eng. Prog.* **1952**, *48*, 89–94.
34. Leung, L.S.; Jones, P.J. Flow of gas—Solid mixtures in standpipes. A review. *Powder Technol.* **1978**, *20*, 145–160. [[CrossRef](#)]
35. Ozahi, E.; Gundogdu, M.Y.; Carpinlioglu, M.Ö. A modification on Ergun’s correlation for use in cylindrical packed beds with non-spherical particles. *Adv. Powder Technol.* **2008**, *19*, 369–381. [[CrossRef](#)]



© 2018 by the authors. Licensee MDPI, Basel, Switzerland. This article is an open access article distributed under the terms and conditions of the Creative Commons Attribution (CC BY) license (<http://creativecommons.org/licenses/by/4.0/>).